Periodic photon-magnon blockade in an optomagnonic system with chiral exceptional points

Zhong-Hui Yuan,[1] Yong-Jian Chen,[1] Jin-Xuan Han,[1] Jin-Lei Wu,[2] Wei-Qi Li,[1] Yan Xia,[3]
Yong-Yuan Jiang,[1] and Jie Song ©[1,4,5,6,*]

[1]*School of Physics, Harbin Institute of Technology, Harbin 150001, China*
[2]*School of Physics and Microelectronics, Zhengzhou University, Zhengzhou, Henan 450001, People's Republic of China*
[3]*Department of Physics, Fuzhou University, Fuzhou 350002, China*
[4]*Key Laboratory of Micro-Nano Optoelectronic Information System, Ministry of Industry and Information Technology, Harbin 150001, China*
[5]*Key Laboratory of Micro-Optics and Photonic Technology of Heilongjiang Province, Harbin Institute of Technology, Harbin 150001, China*
[6]*Collaborative Innovation Center of Extreme Optics, Shanxi University, Taiyuan, Shanxi 030006, People's Republic of China*

We present a straightforward approach for achieving periodic photon-magnon blockade in a hybrid opto-magnonics system, wherein a single optomagnonic resonator is connected to two nanotips via chiral exceptional points (EPs). In non-Hermitian systems, the eigenvalues of the cavity optomagnonics system coalesce at the EPs. We explore the controllable generation of the photon-magnon antibunching effect by modulating the relative angle between the nanotips. Furthermore, we demonstrate that concurrent photon-magnon blockade can be realized without necessitating operation in the strong-coupling regime. In the weak-driving regime, our findings indicate that the photon-magnon blockade is more resilient to the Kerr nonlinearity of both the photon and magnon modes. Additionally, we reveal the versatile tunability of photon-magnon statistics by manipulating the system towards or away from EPs. These characteristics suggest a potential technique for adjustable single photon-magnon sources and a transition from antibunching to bunching in light switches.

I. INTRODUCTION

Recently, the study of hybrid optomagnonics system has played a crucial role in advancing quantum technologies [1–9]. By integrating optical photons with spin waves (magnons), hybrid optomagnonics system can offer multitasking capabilities beyond the reach of individual components [10–14]. Owing to recent advancements in ferromagnetic materials, yttrium iron garnet (YIG) spheres have found applications in diverse systems across various disciplines [15,16]. Specifically, YIG spheres can function as essential components of hybrid optomagnonic systems when interfaced with superconducting qubits or photons [17]. These hybrid optomagnonic systems leverage the high spin density and low dissipation rate of YIG spheres [18–23], with the YIG sphere hosting magnetic excitations and, through whispering-gallery-modes (WGMs) [24], functioning as the optical cavity. The optomagnonic coupling mechanism relies on the Faraday effect, in which the angle of light polarization changes as it propagates through a magnetic material. Over the past decades, numerous investigations have demonstrated the promise of this approach by showcasing coupling between optical modes and magnons.

The study of magneto-optical effect setups also enables in-depth examination of quantum phenomena in hybrid optomagnonic systems, allowing for the observation of rich quantum effects [25–30]. Photon-magnon blockade (PMB), a typical pure quantum phenomenon, has been investigated in analogy with Coulomb blockade [31] and phonon blockade [32–39]. PMB has emerged as a vital aspect in exploring quantum properties of hybrid optomagnonic systems [40–46]. Photon blockade in a $\mathcal{PT}$-symmetric optomechanical system [47], as well as in an optomagnonic system, has been separately investigated. Magnon blockade via a hybrid ferromagnet-superconductor system with two qubits was studied in Ref. [29]. In quantum devices employing hybrid optomechanical systems, single excitation levels are crucial, and the simultaneous blockade of photons and magnons warrants further investigation.

As a key step toward implementing periodic photon-magnon blockade, unique features of non-Hermitian systems have been achieved in various experimental settings [48–52]. Concurrently, the properties and applications of exceptional points (EPs) have garnered significant interest in recent years [53–56]. The periodic emergence of EPs has been observed by coupling WGM microresonators with two external nanotips [57–59]. Building on these experiments, periodic photon-magnon blockade can be achieved by adjusting the relative positions of nanotips along the resonator's circumference [60–63]. Furthermore, exceptional photon blockade via chiral exceptional points has been explored in Ref. [64], presenting unique opportunities for creating and utilizing various single-photon quantum EP devices. By tuning the relative angle of the two nanotips, quantum correlations of photons can be effectively controlled, transitioning from antibunching to bunching regimes or vice versa. Simultaneously, we demonstrate that concurrent photon-

---
*jsong@hit.edu.cn

magnon blockade can be achieved in optomagnonic systems.

In this work, we introduce an experimentally feasible approach to achieving simultaneous photon-magnon blockade in hybrid optomagnonic systems without the need for strong-coupling regimes [65]. Our proposal is based on a meticulously designed hybrid device, where a YIG resonator, coupled to two nanotips, is coherently driven by an input field. Distinct from the microwave regime, where the interaction occurs between microwave photons and magnons, the optomagnonic coupling in the optical case is a three-particle process. Due to the optical photon frequency being in the terahertz range and magnons in the gigahertz range, the optomagnonic coupling in the optical case stems from the Faraday effect, a magneto-optical phenomenon. By carefully positioning the nanotips, the periodic emergence of EPs can be implemented in this system. The relative angle of the nanotips induces asymmetric backscattering, leading to a periodic photon-magnon antibunching effect. Notably, we demonstrate that the PMB is tunable by simply adjusting the relative angle of the nanotips. We also show that EPs not only result in perfect spectral overlap between resonances but force the two corresponding modes to become identical. Our findings confirm that applying two external nanotips to a single YIG sphere, along with the destructive interference between different excitation paths, suppresses two photon-magnon excitation, resulting in the photon-magnon blockade effect. Significantly, we examine the impact of photon and magnon Kerr-nonlinear strength on the antibunching characteristics of the hybrid optomagnonic system in both weak and strong magnon Kerr-nonlinear scenarios. We demonstrate that introducing asymmetric coupling enables a more robust PMB compared with cases without non-Hermitian terms. Our scheme does not necessitate any optical gain or loss or complex refractive index modulation and is well within current experimental capabilities. Consequently, our approach serves as a guideline for hybrid optomagnonic systems to achieve robust PMB, ensuring the development of high-quality and efficient single photon-magnon sources.

II. SYSTEM AND HAMILTONIAN

A. System and Hamiltonian

We consider a system comprising a YIG microresonator coupled to two silica nanotips, fabricated by wet etching a tapered fiber (see Fig. 1). The system is driven by a weak pump field with frequency ω_l. Consequently, both the homogeneous Kittel spin-wave (magnon) mode and the optical WGMs can be excited in the YIG resonator. The associated coupling dynamics rely on the Faraday effect, where the polarization direction of light changes as it propagates through magnetic material. The nanotips are positioned in the evanescent field of the YIG resonator, and their locations can be adjusted using a nanopositioner. We assume that both optical clockwise (CW) and counterclockwise (CCW) modes are simultaneously excited in the resonator, where they couple with the spin. The Hamiltonian of an ideal hybrid cavity optomagnonics system is given by

$$H = H_m + H_o + \boldsymbol{H}_b^{an} + H_{mo}. \qquad (1)$$
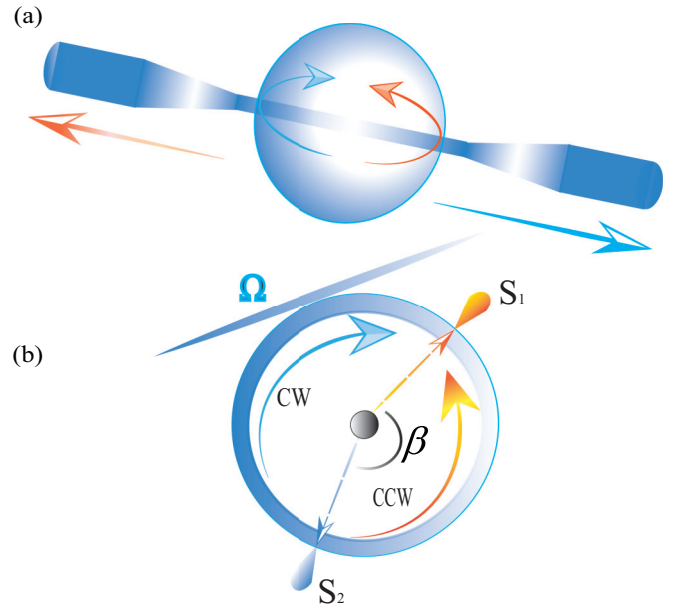
FIG. 1. Schematic diagram of the cavity optomagnonic system consisting of a YIG sphere coupled with two nanotips. An external magnetic field M is applied along the z direction. The homogeneous magnon mode couples to the optical modes with strength g_j. The relative angle between the two nanotips $S_{1,2}$ is denoted β, and the scattering rate of backscattering from the CW (CCW) to CCW (CW) mode is characterized by $J_{12,21}$.

H_m represents the free Hamiltonian of the YIG sphere, while H_o denotes the free Hamiltonian of the counterclockwise (CCW) and clockwise (CW) modes. $\boldsymbol{H}_b^{an}$ is the anisotropy magnetic field. H_{mo} is the interaction Hamiltonian between the CCW (CW) mode and the magnon mode. The free Hamiltonian of the magnon mode, which includes the Zeeman energy and the magnetocrystalline anisotropy energy, can be expressed as follows [15]:

$$H_m = -\int \boldsymbol{M}_b \cdot \boldsymbol{B}_0 d\tau - \frac{\mu_0}{2} \int \boldsymbol{M}_b \cdot \boldsymbol{H}_b^{an} d\tau, \qquad (2)$$

where $\boldsymbol{B}_0 = B_0 \boldsymbol{e}_z$ represents the static magnetic field in the z direction, which is used for magnetizing the YIG sphere. Here, $\boldsymbol{e}_{i=x,y,z}$ are the three orthogonal unit vectors, and $\boldsymbol{M}_b = \hbar \gamma_g \boldsymbol{S}_b / V_{\text{YIG}} \equiv (M_x^b, M_y^b, M_z^b)$ denotes the magnetization of the Kittel mode in the YIG sphere. When the bias magnetic field is applied along the YIG sphere's crystal axis, the anisotropic field can be described as

$$\boldsymbol{H}_b^{an} = \frac{2\hbar \gamma_g S_z^b K_{an}^b}{\mu_0 M_s^2 V_{\text{YIG}}} \boldsymbol{e}_z, \qquad (3)$$

where K_{an}^b represents the dominant first-order anisotropy coefficient, M_s is the saturation magnetization, γ_g refers to the gyromagnetic ratio, V_{YIG} is the volume of the YIG sphere, and $\boldsymbol{S}_b \equiv (S_x^b, S_y^b, S_z^b)$ denotes the collective spin operator of the Kittel mode. The Holstein-Primakoff transformations for the two modes are provided by [66]

$$S_z = S - m^\dagger m,$$
$$S^\dagger = m\sqrt{2S - m^\dagger m},$$
$$S^- = m^\dagger \sqrt{2S - m^\dagger m}, \qquad (4)$$

where S is the total spin the number of the YIG sphere, and $S_o^\pm \equiv S_o^x \pm S_o^y$. In this case, the macroscopic spin operator can be related to the creation operator $m^\dagger$ and annihilation operator m of the magnon at frequency ω_m. The Hamiltonian of the H_m can be written as

$$H_m = \omega_m m^\dagger m + \chi_m m^\dagger m^\dagger mm, \quad (5)$$

where $\omega_m = \gamma_g B_0$ denotes the angular frequency of the magnon mode and the Kerr-nonlinear strength of the magnon mode is $\chi_m = -2\hbar\gamma_g^2 K_{an}^b/M^2 V_{YIG}$.

The free Hamiltonian of the optical WGMs can be expressed as follows [67,68]:

$$H_o = \int d\mathbf{r}\left[\sum_{ij}\frac{\epsilon_o(M_s)}{2}\mathbf{E}_i(\mathbf{r},t)\mathbf{E}_j^*(\mathbf{r},t) + \frac{1}{2\mu_0}|\mathbf{B}_L|^2\right]. \quad (6)$$

The electric field is easily quantized, $\mathbf{E}_i(\mathbf{r},t) \rightarrow \sum_i \mathbf{E}_i(\mathbf{r})a_i(t)$, where $\mathbf{E}_i(\mathbf{r})$ indicates the ith eigenmode of the electric field and $\mathbf{B}_L$ is the ac contribution due to light at optical frequencies, and $\varepsilon_o(\mu_0)$ represents the vacuum permittivity (permeability). By neglecting the constant term, the single-mode electromagnetic field can be quantized as $H_o = \hbar\omega_j a_j^\dagger a_j (j = 1, 2)$, with a_j ($a_j^\dagger$) signifying the annihilation (creation) operators of the jth optical mode with frequency ω_j.

In a Faraday active material, the electromagnetic energy is altered by the coupling between the electric field and the magnetization [69]:

$$H_{mo} = -i\frac{\theta_F \lambda_n}{2\pi}\frac{\varepsilon_o \varepsilon}{2}\int d\mathbf{r} \mathbf{M}_b(\mathbf{r},t) \cdot [\mathbf{E}_i(\mathbf{r},t) \times \mathbf{E}_j^*(\mathbf{r},t)], \quad (7)$$

where $\mathbf{M}_b(\mathbf{r},t)$ denotes the local magnetization in units of the saturation magnetization M_s, and we have used the complex representation of the electric field, $\theta_F = \omega f M_s/2c\sqrt{\varepsilon}$, depends on the frequency ω, the vacuum speed of light c, and the constant f, which is related to the Faraday rotation coefficient in the material [70]. Here, ε represents the relative permittivity, and $n = \sqrt{\varepsilon/\varepsilon_o}$ refers to the refractive index. Equation (7) couples the spin density in the magnetic material with the optical spin density (OSD), which embodies the spin angular-momentum density conveyed by the light field. Quantizing Eq. (7) results in the optomagnonic Hamiltonian. This coupling is parametric, linking one local spin operator to two photon operators.

We consider the coupling of the optical fields (optical mode) to spin-wave excitations (magnon mode). The magnetization requires more careful consideration, since $\mathbf{M}_b(\mathbf{r},t)$ depends on the local spin operator which, in general, cannot be written as a linear combination of bosonic modes. Based on the low-temperature approximation that makes this problem solvable [71–74]. Specifically, we assume that the total number of flipped spins in the system is small compared with the total number of spins. In this case

$$\frac{\langle \sum_i (a_i^\dagger a_i)\rangle}{2S} \ll 1,$$

where S is the total spin. For small deviations $|\delta\mathbf{M}| \ll 1$ [66], we can express these in terms of harmonic oscillators (magnon modes). Quantizing $\mathbf{E}_i(\mathbf{r},t) \rightarrow \sum_i \mathbf{E}_i(\mathbf{r})a_i(t)$, from Eq. (7)

we obtain the coupling Hamiltonian [67,68]

$$H_{mo} = \hbar \sum_{ij\gamma} \mathbf{S}_b G_{ij}^\gamma a_i^\dagger a_j + \text{H.c.}, \quad (8)$$

with

$$G_{ij}^\gamma = -\frac{i}{4}\varepsilon_o f \frac{M_s}{2}[\mathbf{E}_j^*(\mathbf{r}) \times \mathbf{E}_i(\mathbf{r})] \quad (9)$$

being the local optomagnonic coupling. The Greek subindices indicate the respective magnon and photon modes that are coupled. For two degenerate modes at frequency ω_j, using Eq. (8), we observe that the frequency dependence cancels out, resulting in a simplified form for the optomagnonic Hamiltonian [67]:

$$H_{mo} = \hbar G \hat{S}_x(a_1^\dagger a_1 + a_2^\dagger a_2), \quad (10)$$

where $G = \frac{1}{S}\frac{c\theta_F}{4\sqrt{\varepsilon}}$. We can represent the spin as a harmonic oscillator in the usual manner, with $\hat{S}_x \approx \sqrt{S/2}(m + m^\dagger)$. Using Eq. (9), we evaluate the coupling between optical WGMs and magnon modes in a YIG sphere containing a magnetic vortex, specifically focusing on magnonic modes localized at the vortex. Such a model of the hybrid cavity optomagnonical system can be described by a non-Hermitian interaction Hamiltonian

$$\begin{aligned} H_1 &= \omega_1 a_1^\dagger a_1 + \omega_2 a_2^\dagger a_2 + \omega_m m^\dagger m + \chi_m m^\dagger m^\dagger mm \\ &+ \chi_1 a_1^\dagger a_1^\dagger a_1 a_1 + \chi_2 a_2^\dagger a_2^\dagger a_2 a_2 + g_1 a_1^\dagger a_1(m^\dagger + m) \\ &+ g_2 a_2^\dagger a_2(m^\dagger + m) + J_{12}a_1^\dagger a_2 + J_{21}a_1 a_2^\dagger \\ &+ \Omega(a_1^\dagger e^{-i\omega_l t} + a_1 e^{i\omega_l t}). \end{aligned} \quad (11)$$

Then, in the rotating frame with respect to the driving laser field $V = \exp[-i\omega_l t(a_1^\dagger a_1 + a_2^\dagger a_2)]$, the total Hamiltonian of the system can be reduced to [75]

$$\begin{aligned} H' &= \Delta_1 a_1^\dagger a_1 + \Delta_2 a_2^\dagger a_2 + \omega_m m^\dagger m + \chi_m m^\dagger m^\dagger mm \\ &+ \chi_1 a_1^\dagger a_1^\dagger a_1 a_1 + \chi_2 a_2^\dagger a_2^\dagger a_2 a_2 + g_1 a_1^\dagger a_1(m^\dagger + m) \\ &+ g_2 a_2^\dagger a_2(m^\dagger + m) + J_{12}a_1^\dagger a_2 + J_{21}a_1 a_2^\dagger \\ &+ \Omega(a_1^\dagger + a_1). \end{aligned} \quad (12)$$

Specifically, there is coherent coupling between the CW (CCW) mode a_1 (a_2) and the magnon mode m, corresponding to coupling strengths $g_j = G\sqrt{S/2}$ and the detuning of the optical mode is given by $\Delta_j = \omega_j - \omega_l$ ($j = 1, 2$). Meanwhile, the scattering rate of backscattering from the CW (CCW) to CCW (CW) mode results in non-Hermitian coupling, with coupling strengths J_{12} (J_{21}). The Kerr-nonlinear strength of the photon modes is $\chi_j = 3\hbar\omega^2\chi^{(3)}/4\varepsilon_0\varepsilon_r^2 V_{eff}$.

III. ENERGY AND TRANSMISSION SPECTRA

The non-Hermitian optical coupling between a_1 and a_2 can be described by the scattering from the clockwise (CW) to the counterclockwise (CCW) mode, and vice versa, with

$$J_{12(21)} = \epsilon_1 + \epsilon_2 e^{\pm i\sigma\beta}. \quad (13)$$

Assuming the frequency of the CW mode is equal to the CCW mode, i.e., $\omega_1 = \omega_2 = \omega$, the detuning of the optical mode is given by $\Delta_j = \omega_j - \omega_l$, and the effective detuning is $\Delta = \Delta_j + \text{Re}(\epsilon_1 + \epsilon_2)$. ϵ_1 (ϵ_2) represents the perturbation
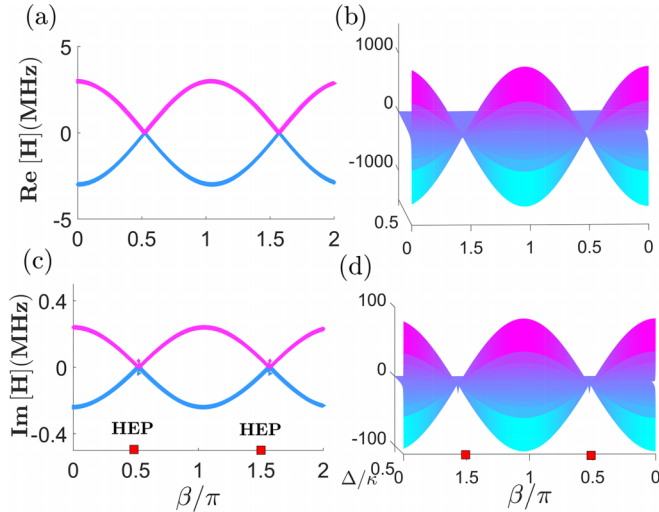
FIG. 2. The eigenvalue splitting varies with the angle β. Re (Im) denotes the real (imaginary) part of the eigenvalues.

FIG. 3. Transmission spectra of the CW mode as the relative phase angle β between the nanotips was varied frequency detuning Δ. β increased continuously from top to bottom.

introduced by the nanotip 1 (2), which can be adjusted by controlling the distance between the nanotip and the resonator. σ and β denote the azimuthal mode number and the relative angle of the nanoscatterers, respectively. Steering of the angle β can bring the system to EPs, as already observed experimentally [48,76]. The purpose of our work here is to show the role of EPs achieved by tuning β in the photon-magnon blockade process [48,76]. For $J_{12} = J_{21} = 0$, i.e., when the two nanoscatterers are absent, the Hamiltonian H' has two orthogonal eigenstates with the same frequency. For $J_{12} = 0$ or $J_{21} = 0$, H' has only one eigenvalue and one eigenvector, indicating the emergence of an EP. In this case, when $J_{12} = 0$, we have

$$\beta_{EPs} = \frac{l\pi}{2\sigma} \pm \frac{\arg(\epsilon_1) - \arg(\epsilon_2)}{2\sigma}, \quad l = \pm 1, \pm 3, \ldots, \quad (14)$$

where $\epsilon_1/\epsilon_1^* \neq \epsilon_2/\epsilon_2^*$ can be achieved in experiments by tuning the distance between the resonator and the particles, and $\pm$ corresponds to $J_{12} = 0$ or $J_{21} = 0$.

As depicted in Figs. 2(a)–2(c), the special effect Hamiltonian H' demonstrates that the positions of the Hamiltonian EPs (HEPs) coincide with the values of β. By modulating β, the split eigenspectra gradually approach and merge into a single point at $\beta = n\pi/2$ ($n = 1, 3$), revealing the position of the Liouville singularity. Furthermore, due to the circular structure of the WGM cavity, the system's singularity appears periodically as the relative angular position is adjusted. We plot the energy spectrum vs the relative phase angle β and the frequency detuning of the optical mode Δ in Figs. 2(b)–2(d). The EPs also exhibit a completely asymmetric coupling between the CW and CCW modes, meaning that light can only scatter from the CCW mode to the CW mode when $J_{12} = 0$ and $J_{21} \neq 0$, or from the CW mode to the CCW mode when $J_{12} \neq 0$ and $J_{21} = 0$. Since the coupling between optical modes is dependent on the relative angular position β of the two nanoscatterers, adjusting β allows the system to be placed at EPs.

The characteristics of EPs can also be clearly observed in the transmission spectra shown in Fig. 3, where two spectrally separated resonance modes start to overlap. Additionally, under weak-driving conditions, the occurrence of PMB is intimately related to the resonance mode in the excitation spectrum. An EP not only results in a perfect spectral overlap between resonances but also forces the two corresponding modes to become identical. Owing to asymmetric backscattering near an EP, the two modes become chiral, i.e., both modes possess a dominant contribution (CW or CCW). Moreover, they are primarily copropagating, meaning that the dominant contribution is the same for both modes. For instance, both modes can have a large CCW component and only a small CW component. As the system approaches the EP, the CW component decreases even further. At the EP, the CW component vanishes due to destructive interference, and both modes, considered as two-dimensional vectors (CCW or CW = 0), become collinear. Consequently, only one independent eigenvector exists at the EPs.
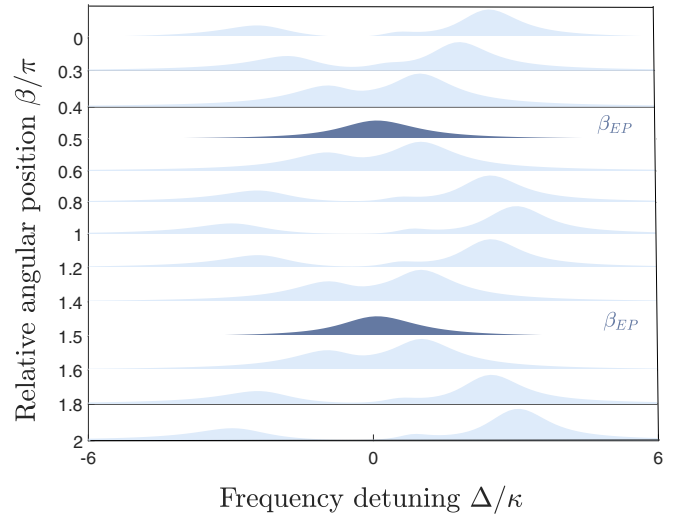
On the other hand, the photon antibunching of the CW mode is linked to the quantum interference between multiple transition paths, as shown in Fig. 4: $|0, 0, 0\rangle \xrightarrow{\Omega} |1, 0, 0\rangle \xrightarrow{\Omega} |2, 0, 0\rangle$ and $|1, 0, 0\rangle \xrightarrow{J_{12}} |0, 1, 0\rangle \xrightarrow{\Omega} |1, 1, 0\rangle \xrightarrow{\sqrt{2}J_{21}} |2, 0, 0\rangle$. Due to destructive interference, the two-photon state $|2, 0, 0\rangle$ cannot be occupied. Therefore, the ideal photon blockade effect can be achieved in the hybrid optomagnonics system.

IV. ANALYTICAL SOLUTION AND MASTER EQUATION NUMERICAL SIMULATION

In this section, we investigate the photon-magnon blockade effect in a non-Hermitian cavity optomagnonics system by both analytically and numerically calculating the equal-time second-order correlation function.

A. Analytical solution

To determine the specific conditions for photon-magnon antibunching, we conveniently employ the probability
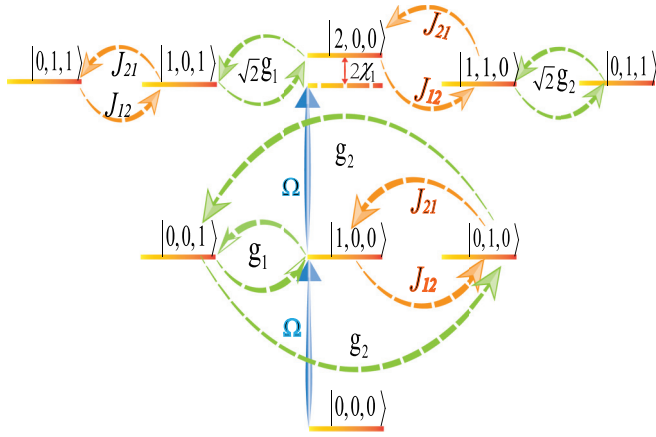
FIG. 4. The energy levels of the system within the few-photon subspace can be represented by states labeled as $|n_{a_1}, n_{a_2}, n_m\rangle$, where n_{a_1} and n_{a_2} denote the photon numbers of the CW and CCW modes, and n_m indicates the magnon mode. The optomagnonic coupling between the optical modes and the Kittel mode, as well as the non-Hermitian coupling between the CCW optical mode and the CW mode, contribute to the destructive interference within the system. Consequently, the path of quantum destructive interference is expanded.

amplitude method for analytically calculating the second-order correlation functions. By considering the dissipation of the two cavities and the magnon mode, we utilize an effective non-Hermitian Hamiltonian to describe the system's evolution.

$$H_{\text{eff}} = H' - i\frac{\kappa_1}{2}a_1^\dagger a_1 - i\frac{\kappa_2}{2}a_2^\dagger a_2 - i\frac{\kappa_m}{2}m^\dagger m. \quad (15)$$

In this context, κ_1, κ_2, and κ_m denote the decay rates of the photons and the magnon mode. To streamline calculations, we set $\Delta_1 = \Delta_2 = \Delta$ and $\kappa_1 = \kappa_2 = \kappa_m = \kappa$, and assume the system is initially in its ground state. For a sufficiently weak pumping field, only a few photons can be excited, constraining the total photon number within the low-excitation subspace up to two. The dynamic evolution of the optical components is computed using the Schrödinger equation $i\partial|\psi(t)\rangle/\partial t = H_{\text{eff}}|\psi(t)\rangle$, where $|\psi(t)\rangle$ represents the time-dependent photon and magnon state. Consequently, a general wave function for the system can be expanded within the few-photon subspace as follows:

$$\begin{aligned}
|\psi(t)\rangle = {}&C_{000}|0,0,0\rangle + C_{010}|0,1,0\rangle + C_{001}|0,0,1\rangle \\
&+ C_{100}|1,0,0\rangle + C_{002}|0,0,2\rangle + C_{110}|1,1,0\rangle \\
&+ C_{101}|1,0,1\rangle + C_{011}|0,1,1\rangle. \quad (16)
\end{aligned}$$

Here, C_{n_1,n_2,n_m} represents the probability amplitude, and $|C_{n_1,n_2,n_m}|^2$ indicates the occupation probability of state $|n_1, n_2, n_m\rangle$, with n_1, n_2, n_m denoting the number of photons and magnons, respectively. This formulation leads to a set of linear differential equations for the probability amplitudes:

$$i\dot{C}_{000} = \Omega C_{100},$$

$$\begin{aligned}
i\dot{C}_{100} = {}&\left(\Delta_1 - i\frac{\kappa_1}{2}\right)C_{100} + \sqrt{2}g_1 C_{001} + J_{21}C_{010} + \Omega \\
&+ \sqrt{2}\Omega C_{200},
\end{aligned}$$

$$i\dot{C}_{010} = \left(\Delta_2 - i\frac{\kappa_2}{2}\right)C_{010} + g_2 C_{001} + J_{12}C_{100} + \Omega C_{110},$$

$$i\dot{C}_{001} = \left(\Delta_m - i\frac{\kappa_m}{2}\right)C_{001} + g_1 C_{100} + g_2 C_{010} + \Omega C_{101},$$

$$\begin{aligned}
i\dot{C}_{200} = {}&2\left(\Delta_1 - i\frac{\kappa_1}{2} + 2K\right)C_{200} + \sqrt{2}g_1 C_{101} + \sqrt{2}J_{12}C_{110} \\
&+ \sqrt{2}\Omega C_{100},
\end{aligned}$$

$$\begin{aligned}
i\dot{C}_{101} = {}&\left(\Delta_1 + \Delta_m - i\frac{\kappa_1}{2} - i\frac{\kappa_m}{2}\right)C_{101} + \sqrt{2}g_1 C_{200} + g_2 C_{110} \\
&+ J_{21}C_{011} + \Omega C_{001},
\end{aligned}$$

$$i\dot{C}_{011} = \left(\Delta_1 + \Delta_2 - i\frac{\kappa_1}{2} - i\frac{\kappa_2}{2}\right)C_{011} + g_1 C_{110} + J_{12}C_{101},$$

$$\begin{aligned}
i\dot{C}_{110} = {}&\left(\Delta_1 + \Delta_2 - i\frac{\kappa_1}{2} - i\frac{\kappa_2}{2}\right)C_{110} + \sqrt{2}J_{21}C_{200} + g_1 C_{011} \\
&+ g_2 C_{110} + \Omega C_{010}. \quad (17)
\end{aligned}$$

Under the weak driving condition, we observe that $\{|C_{200}|, |C_{101}|, |C_{011}|, |C_{110}|\} \ll \{|C_{100}|, |C_{010}|, |C_{001}|\} \ll |C_{000}|$, allowing us to approximate $C_{000} \approx 1$. By neglecting higher-order terms with respect to Ω, we can approximate the probability amplitudes for the steady state. Consequently, the self-correlation function of the photon-magnon blockade in the steady state can be analytically derived using Eqs. (15)–(17):

$$\begin{aligned}
g_{a_1}^{(2)}(0) &= \frac{\langle a_1^\dagger a_1^\dagger a_1 a_1\rangle}{\langle a_1^\dagger a_1\rangle^2} \\
&= \frac{2|C_{200}|^2}{(|C_{100}|^2 + |C_{101}|^2 + 2|C_{110}|^2)^2}. \quad (18)
\end{aligned}$$

Specifically, a perfect photon-magnon blockade effect in the cavity optomagnonics system can be characterized by the condition $|C_{200}| = 0$.

B. Master equation numerical simulation

To move forward, it is crucial to understand how to describe the hybrid system within the framework of open quantum mechanics. We concentrate on the generation of blockade among the magnon and photon modes at chiral exceptional points. First, the evolution of the hybrid system can be assessed using the master equation [52,77–79]

$$\frac{\partial \rho}{\partial t} = -i[\mathcal{H}_1, \rho] - i\{\mathcal{H}_2, \rho\} + 2i\langle\mathcal{H}_2\rangle\rho + \sum_j \mathcal{D}(\rho, \hat{A}_j). \quad (19)$$

In this equation, ρ represents the system's density matrix, while $\mathcal{H}_1$ ($\mathcal{H}_2$) is a Hermitian (non-Hermitian) operator obtained by recasting the effective Hamiltonian as $\mathcal{H}_1 \equiv (H' + H'^\dagger)/2$ [$\mathcal{H}_2 \equiv (H' - H'^\dagger)/2$] and $\sum_j \mathcal{D}(\rho, \hat{A}_j) = \hat{A}_j\rho\hat{A}_j^\dagger - \hat{A}_j^\dagger\hat{A}_j\rho/2 - \rho\hat{A}_j^\dagger\hat{A}_j/2$ represents the Lindblad operator for the system operator $\hat{A}_j = \sqrt{\kappa}o(o = a_j, m)$. Furthermore, $\langle\mathcal{H}_2\rangle = \text{tr}(\rho\mathcal{H}_2)$, and the brackets $[\cdot]$ and $\cdot$ denote the commutator and anticommutator, respectively. Notably, the resulting equation is nonlinear in the quantum state ρ due to the addition of the third term, which ensures that $\text{tr}(\rho) = 1$. In this section, we discuss the robustness of the cavity
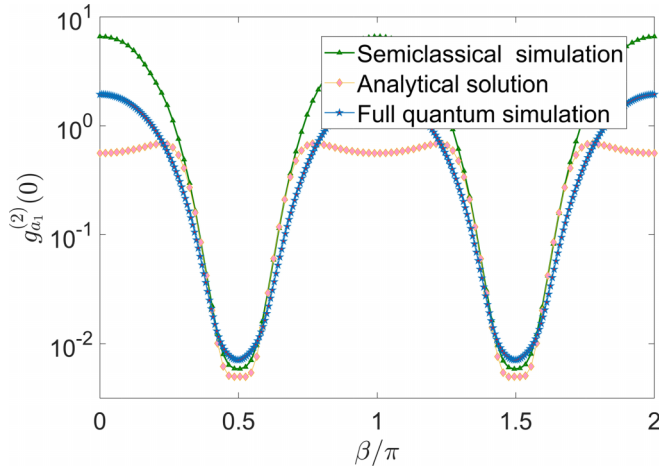
FIG. 5. The equal-time second-order correlation functions $g_{a_1}^{(2)}(0)$ versus the relative phase angle β. The parameters are set as $\kappa_1 = \kappa_2 = \kappa_m$, $\Delta_j = \omega_m = 0.5\kappa_1$, $g_1 = g_2 = 0.3\kappa_1$, $\chi_1 = 10\kappa_1$, $\chi_m = 0.1\kappa_1$, and $\Omega = 0.1\kappa_1$.

optomagnonics system's photon or magnon blockade against the phase angle β. Two dominant influencing factors are considered: (i) unexpected magnon-photon coupling g_j/κ_1; (ii) the Kerr-nonlinear strength of the CW mode, CCW mode, and magnon mode. In the long-time limit, the steady-state density matrix ρ_s of the system can be obtained. Simultaneously, the steady-state second-order correlation functions of the CW, CCW, and magnon modes are given by

$$g_m^{(2)}(0) = \frac{\text{Tr}(m^\dagger m^\dagger m m \rho_s)}{[\text{Tr}(m^\dagger m)\rho_s]^2},$$

$$g_{a_j}^{(2)}(0) = \frac{\text{Tr}(a_j^\dagger a_j^\dagger a_j a_j \rho_s)}{[\text{Tr}(a_j^\dagger a_j)\rho_s]^2}. \quad (20)$$

To validate our analysis, we compare the equal-time second-order correlation function of the CW mode as a function of the relative phase angle β using both analytical and numerical methods, as shown in Fig. 5. The analytic solution corresponds to Eq. (18) and the numerical simulation corresponds to Eq. (20). The analytical and numerical results are in strong agreement, confirming the accuracy of our findings. Moreover, we also compare the equal-time second-order correlation function of the CW mode as a function of the relative phase angle β using both semiclassical simulation and full quantum simulation methods. The full quantum master equation is expressed as $\partial \rho / \partial t = -i[\mathcal{H}_1, \rho] + \sum_j \mathcal{D}(\rho, \hat{A}_j) + \mathcal{D}(\rho, \hat{\Gamma})$, where $\hat{\Gamma} = \sqrt{-2i\mathcal{H}_2}$ is the additional jump operator [78,80]. When considering the quantum noise caused by non-Hermitian coupling, the second-order correlation function of the CW is most significantly affected by quantum noise when far away from the exceptional points and is not affected by quantum noise at the EPs (Fig. 5). When the system is located at exceptional points, the two optical modes are merged into a single mode. The light field energy is mainly limited in the CW mode, and the quantum correlation is mainly influenced by the CW mode. At this time, the CW mode has good robustness to the quantum noise, so the quantum noise does not influence the quantum correlation at the EPs. The
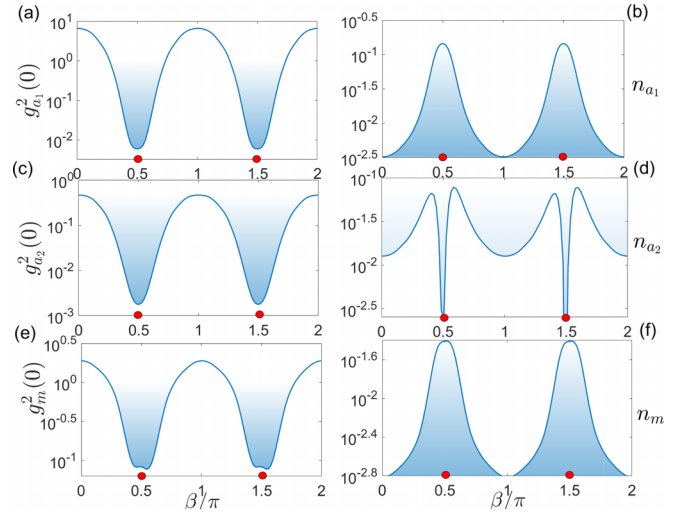
FIG. 6. The equal-time second-order correlation functions of the CW, CCW, and magnon modes are plotted as a function of the relative phase angle β. On the left, the blue lines represent the numerical results of (a) $g_{a_1}^{(2)}(0)$, while the purple line and the yellow line correspond to (c) $g_{a_2}^{(2)}(0)$ and (e) $g_m^{(2)}(0)$, respectively. On the right, the blue lines depict the photon number (b) n_{a_1}, and the purple line and the yellow line represent the photon numbers of (d) n_{a_2} and (f) n_m, respectively. The parameters are set as $\kappa_1 = \kappa_2 = \kappa_m$, $\Delta_j = \omega_m = 0.5\kappa_1$, $g_1 = g_2 = 0.3\kappa_1$, $\chi_1 = 10\kappa_1$, $\chi_m = 1 \times 10^{-10}\kappa_1$, and $\Omega = 0.1\kappa_1$.

second-order correlation function of the CW mode exhibits the lowest values of $g_{a_1}^{(2)}(0) \approx 0.001$. When the system is far away from the exceptional points, the quantum correlation is influenced by two optical modes, and the CW mode is sensitive to quantum noise, so the quantum noise has a significant influence on the quantum correlation at the distance from the exceptional points.

V. PHOTON-MAGNON BLOCKADE WITH CHIRAL EXCEPTIONAL POINTS

A. Photon-magnon blockade in the weak-driving regime

In this section, we examine the characteristics of the antibunching effect for photons and magnons in a hybrid cavity optomagnonics system operating in the weak-driving regime ($\Omega \ll \kappa_1$). We set the dissipation parameters for photons and magnon as $\kappa_1 = \kappa_2 = \kappa_m$, and the photon driving strength as $\Omega = 0.1\kappa_1$. In the weak-driving limit, where $\Omega \ll \{g_1, g_2, \kappa_1, \kappa_2, \kappa_m\}$, the total excitation number is limited to $N \leqslant 2$. To ensure the accuracy of our numerical results, we truncate the largest number of Hilbert space at three.

To demonstrate the simultaneous photon-magnon blockade in the hybrid optomagnonics system, we plot the second-order correlation function $g_j^{(2)}(0)$ against the relative angle β, as depicted in Figs. 6(a), 6(c), and 6(e). We observe that at $\omega = \omega_l$, the antibunching effect periodically varies with β, and the value of $g_{a_1}^{(2)}(0)$ can reach ≈ 0.001 at exceptional points (EPs). Moreover, the blockade of the counterclockwise (CCW) and magnon modes can also be detected when $\beta = \pi/2$ or $\beta = 3\pi/2$, with $g_{a_2}^{(2)}(0) \approx 0.001$ and $g_m^{(2)}(0) \approx 0.06$. Simultaneously, the average number n_j ($j = a_1, a_2, m$) reach

a local maximum value at EPs, as shown in Figs. 6(b), 6(d), and 6(f). We find that the maximum average photons number of the steady state n_{a_1} and n_{a_2} can reach ≈ 0.25 and ≈ 0.16 and the maximum average magnon number of the steady state n_m can reach ≈ 0.06. Thus, the system can work as an efficient single photon and magnon source device with a large output of photons and magnons.

As illustrated in Fig. 6, we investigate by modulating the phase angle β, the second-order correlation function exhibits the highest values of $g_m^{(2)}(0) \approx 0.1$, $g_{a_1}^{(2)}(0) \approx 3.16$, and $g_{a_2}^{(2)}(0) \approx 0.1$ and the lowest values of $g_m^{(2)}(0) \approx 0.06$, $g_{a_1}^{(2)}(0) \approx 0.001$, and $g_{a_2}^{(2)}(0) \approx 0.003$. "In Fig. 6(e) we observe an interesting phenomenon: in contrast with the true minimum, this local minimum value represents a magnon blockade region. The results indicate the second-order correlation function of magnon blockade when $\beta = 0.45\pi$ and $\beta = 0.55\pi$ is always larger than the one when EPs are at the $\beta = 0.5\pi$. Meanwhile, we can see that the system reaches a steady state after a long evolution time. The magnon blockade effect can also be understood through the theory of unconventional magnon blockade (UMB), which involves quantum interference between multiple transition paths: $|0,0,0\rangle \xrightarrow{\Omega} |1,0,0\rangle \xrightarrow{g_1} |0,0,1\rangle$ and $|0,0,0\rangle \xrightarrow{\Omega} |1,0,0\rangle \xrightarrow{J_{12}} |0,1,0\rangle \xrightarrow{g_2} |0,0,1\rangle$. We find that magnon blockade is facilitated by optomagnonic coupling g_j, external driving field Ω, and non-Hermitian coupling J_{12} and J_{21}. However, the realization of photon blockade mainly depends on the external driving field Ω and non-Hermitian coupling J_{12} and J_{21}. Non-Hermitian coupling plays a distinct role in magnon blockade because it is first employed to transition to the $|0,1,0\rangle$ state. Subsequently, magnon needs to couple to photons using optomagnonic coupling g_j to drive the transition $|0,1,0\rangle \rightarrow |0,0,1\rangle$." This result implies that a coherent laser with a fixed frequency can be transformed into concentrated light with a super-Poissonian distribution by adjusting β. This behavior differs from the quantum correlation change achieved by modifying the driving frequency in conventional photon blockade effects. Thus, phase angle modulation plays a crucial role. Quantum correlation changes spanning three orders of magnitude can be realized at a fixed frequency, making it a promising candidate for novel artificial quantum devices, such as classical-quantum light source converters and antibeam all-optical switches.

To comprehend the physical mechanism underlying this counterintuitive effect and the distinction from the Hermitian case, we examine the excitation pathways illustrated in Fig. 7. At the exceptional points (EPs) of the system, the counterclockwise (CCW) mode couples to the clockwise (CW) mode and vice versa, i.e., $J_{12} = 0$ and $J_{21} \neq 0$ ($J_{12} \neq 0$ and $J_{21} = 0$), resulting in a predominantly CW (CCW) propagating mode. We deduce that at $\omega = \omega_l$, a photon blockade (PB) with strong antibunched single photons arises at EPs, while a bunched stream appears in the Hermitian case, as depicted in Fig. 7(a). Simultaneously, the average number n_{a_1} also shows this feature, as depicted in Fig. 7(b). The value of n_{a_1} can reach ≈ 0.03 at exceptional points (EPs), while the lower panel shows photon-induced tunneling (PIT) in the Hermitian case for $J_{12} = J_{21} = 2\kappa_1$, the average number values can reach ≈ 0.003. Figure 7(c), confirming that the system reaches a
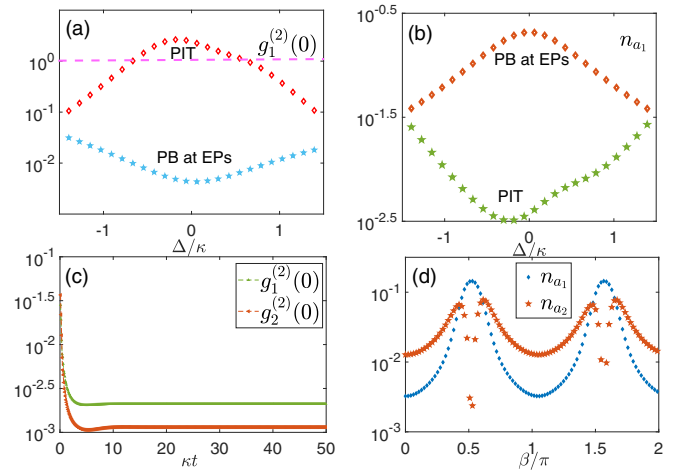
FIG. 7. (a) The equal-time second-order correlation functions $g_{a_1}^{(2)}(0)$ versus the detuning Δ/κ_1 for the non-Hermitian (blue star) and Hermitian (red rhombus) cases. (b) The photon numbers of n_{a_1} versus the detuning Δ/κ_1 for the non-Hermitian (blue star) and Hermitian (red rhombus) cases. (c) The dynamical evolution of the equal-time second-order correlation function with the CW and CCW modes. (d) In the non-Hermitian case, the photon numbers n_{a_1} and n_{a_2} versus the relative phase angle β. The parameters are set as $\kappa_1 = \kappa_2 = \kappa_m$, $\omega_m = 0.5\kappa_1$, $g_1 = g_2 = 0.3\kappa_1$, $\chi_1 = 10\kappa_1$, $\chi_m = 1 \times 10^{-10}\kappa_1$, and $\Omega = 0.1\kappa_1$.

steady state after an extended evolution time, and optimal system parameters yield perfect PB. However, the transition to the $|2,0,0\rangle$ state is governed by J_{21}, which is negligible in a system with CCW drive and in a predominantly CCW mode [see $n_{a_1} \gg n_{a_2} \approx 0$ in Fig. 7(d)].

Moreover, we also study the effect of parameter fluctuations on the equal-time second-order correlation function and show those results in Fig. 8. To further clarify whether the perfect PMB can be achieved periodically by tuning the relative angle of nanotips, we analyze the optimal antibunching effect of the photon and magnon (solid white line in Fig. 8). The minimal value of the $g_{a_1}^{(2)}(0)$ and $g_m^{(2)}(0)$ occurs at $\beta = \pi/2$ and $\beta = 3\pi/2$. And the detuning of optical modes satisfies $\omega = \omega_l$, i.e., $\Delta = 0$. Consequently, the system can absorb only one photon and magnon, leading to photon blockade (PB) [magnon blockade (MB)] and antibunched single photon-magnon pairs with $g_{a_1}^{(2)}(0) \ll 1$ and $g_m^{(2)}(0) \ll 1$. The interplay of EPs and the detuning creates a new type of single-photon blockade effect that takes place at two-photon resonance. This property can be used to construct single-photon devices with frequency-tunable.

B. Photon-magnon blockade in the weak optomagnonic coupling regime

In this section, we explore the impact of optomagnonic coupling strength on the photon (magnon) blockade (PMB) by numerically investigating the evolution of the second-order correlation functions $g_{a_1}^{(2)}(0)$ and $g_{a_2}^{(2)}(0)$ for various relative phase angles β. To more intuitively represent the relationship between the optomagnonic coupling strength, relative phase angle, and the correlation functions of the counterclockwise (CCW) and clockwise (CW) modes, we present the results
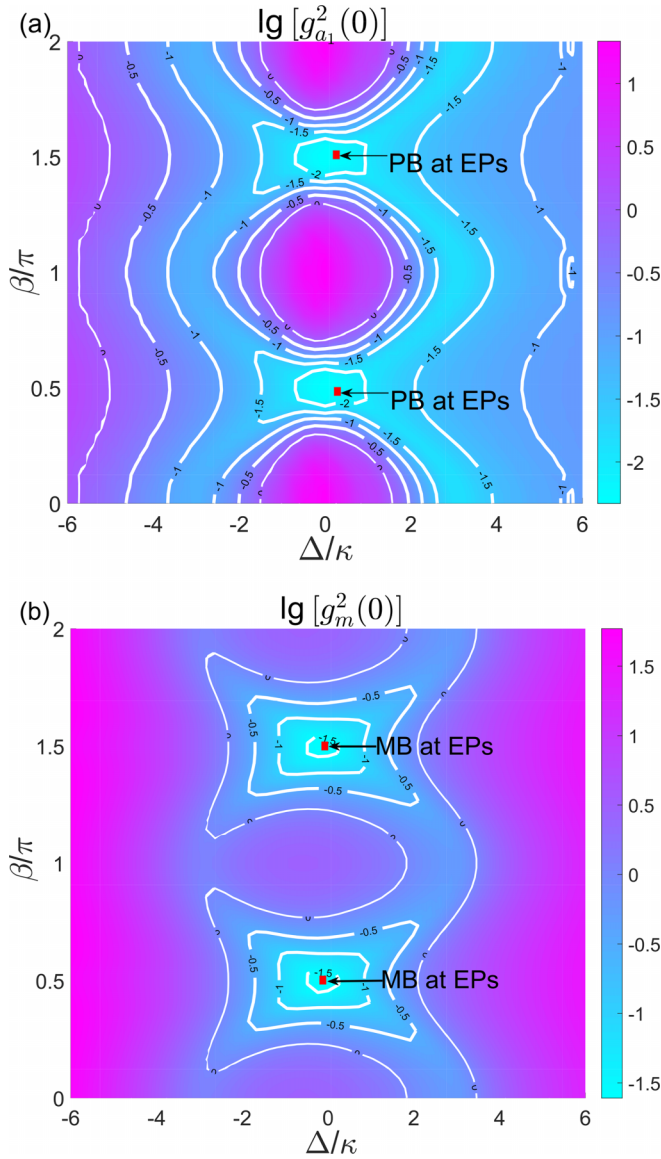
FIG. 8. The equal-time second-order correlation functions (a) $g_{a_1}^{(2)}(0)$ and (b) $g_m^{(2)}(0)$ versus the detuning Δ and the relative phase angle β. The parameters are set as $\kappa_1 = \kappa_2 = \kappa_m$, $\omega_m = 0.5\kappa_1$, $g_1 = g_2 = 0.3\kappa_1$, $\chi_1 = 10\kappa_1$, $\chi_m = 1 \times 10^{-10}\kappa_1$, and $\Omega = 0.1\kappa_1$.

FIG. 9. The equal-time second-order correlation functions (a) $g_{a_1}^{(2)}(0)$ and (b) $g_{a_2}^{(2)}(0)$ versus the optomagnonics coupling strength g_j and the relative phase angle β. The parameters are set as $\kappa_1 = \kappa_2 = \kappa_m$, $\Delta_j = \omega_m = 0.5\kappa_1$, $g_1 = g_2 = 0.3\kappa_1$, $\chi_1 = 10\kappa_1$, $\chi_m = 1 \times 10^{-10}\kappa_1$, and $\Omega = 0.1\kappa_1$.

in Fig. 9. As observed, the photon-magnon antibunching effect can periodically appear under the conditions $\beta = \pi/2$ or $\beta = 3\pi/2$. We find that the second-order correlation functions of the CCW and CW modes reach their minimum values at the exceptional points (EPs). Consequently, the EPs at $\beta = \pi/2$ and $\beta = 3\pi/2$ serve as critical points for determining whether the PMB can undergo periodic variations.

As demonstrated, the photon-magnon antibunching effect can periodically arise by adjusting the relative phase angle β for light with $\omega = \omega_l$. Modulation of the relative phase angle β can induce nearly three orders of magnitude periodic change in the second-order correlation function of the light field. Based on our analysis and discussion, we discover that perfect PMB can be achieved even with weak optomagnonic coupling strength (e.g., $g_j \ll \kappa$). This finding indicates that

the PMB in hybrid optomagnonic systems is more robust to variations in optomagnonic coupling strength.

C. The robustness of the Kerr-nonlinear strength

In this section, we focus on the characteristics of the antibunching effect of photon-magnon interactions in a hybrid optomagnonics quantum system with photon-magnon resonance detuning, i.e., $\Delta_j = \omega_m$. The system exhibits non-Hermitian coupling between the counterclockwise (CCW) and clockwise (CW) modes. We investigate the influence of photon and magnon Kerr-nonlinear strengths on the antibunching characteristics of the system under weak magnon Kerr-nonlinear strength regimes.
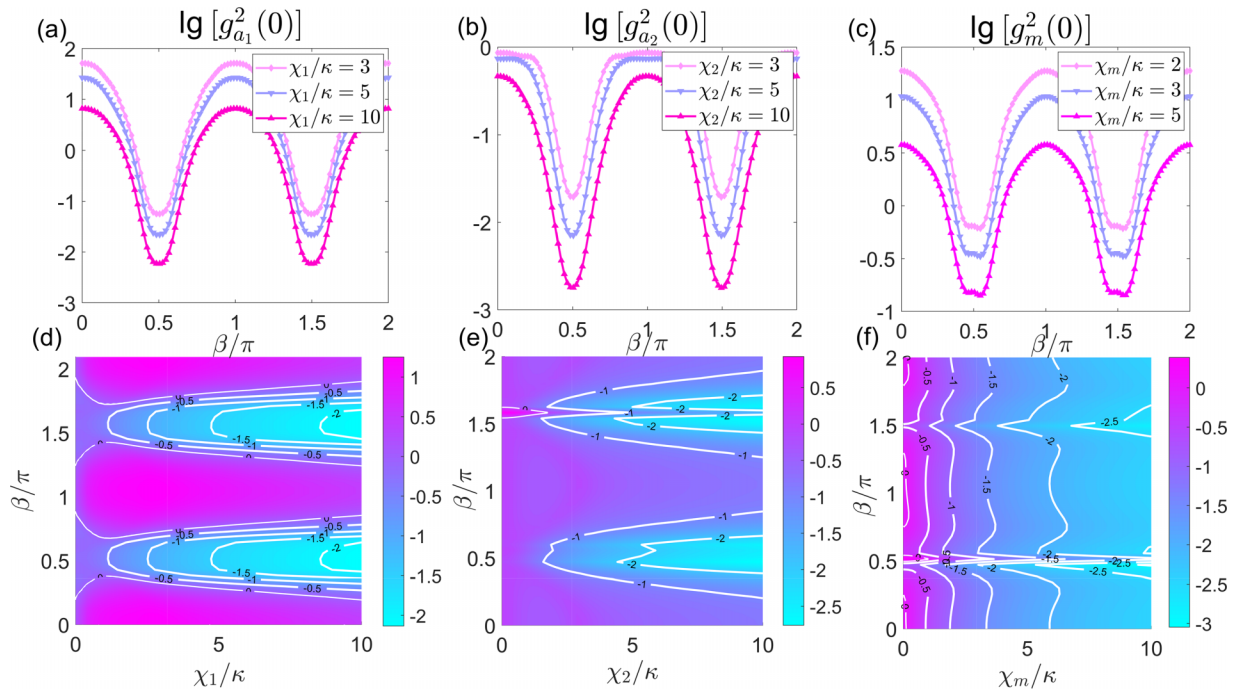
FIG. 10. (upper) The equal-time second-order correlation functions of the CW, CCW, and magnon modes versus the relative phase angle β with different the Kerr-nonlinear strength. (lower) The equal-time second-order correlation functions of the CW, CCW, and magnon modes versus the relative phase angle β and the Kerr-nonlinear strength $\chi_{1,2,m}$. The parameters are set as $\kappa_1 = \kappa_2 = \kappa_m$, $\Delta_j = \omega_m = 0.5\kappa_1$, $g_1 = g_2 = 0.3\kappa_1$, and $\Omega = 0.1\kappa_1$.

In the weak magnon Kerr-nonlinear strength regime, we fix the weak optomagnonic coupling regime ($g_j/\kappa = 0.3$) and the magnon Kerr-nonlinear strength ($\chi_m/\kappa = 10^{-10}$). To further elucidate whether the perfect photon-magnon blockade can be achieved by the CW mode, CCW mode, and magnon mode, we examine Fig. 10(a), which plots the second-order correlation function $g_{a_1}^{(2)}(0)$ as a function of β/π for different Kerr-nonlinear strengths χ_1. The perfect photon blockade can be observed with the increase of Kerr nonlinear strength, e.g., $\chi_1/\kappa = 10$ (the pink line). More intuitively, Fig. 10(d) reveals that, in the presence of the relative angular position difference between the CCW and CW modes, two dips occur; the white lines satisfy the optimal conditions. When the relative angular positions of the CCW and CW modes differ, two additional dips gradually emerge at EPs occurring at $\beta = \pi/2$ or $\beta = 3\pi/2$. Thus, the photon Kerr-nonlinear strength plays a crucial role in controlling the antibunching effect of the CCW mode, providing a method for the preparation of a single-photon source.

Furthermore, in the weak magnon Kerr-nonlinear strength regime, i.e., ($\chi_m/\kappa = 10^{-10}$), we plot the logarithmic scale of the equal-time second-order correlation function $\log_{10}[g_{a_2}^{(2)}(0)]$ as a function of the relative angular position β with different photon Kerr-nonlinear strengths of the CW mode in Fig. 10(b). We find that the equal-time second-order correlation function $g_{a_2}^{(2)}(0)$ exhibits a prominent antibunching effect at $\beta = \pi/2$ or $\beta = 3\pi/2$. For different photon Kerr-nonlinear strengths, it varies monotonically as χ_2/κ increases. To enhance the understanding of this situation, we plot the second-order correlation function $g_{a_2}^{(2)}(0)$ as a function of β/π and the Kerr-nonlinear strength χ_2 in Fig. 10(e). We observe that the strong photon antibunching effect $g_{a_1}^{(2)}(0) \ll 1$ appears

in the curved dark blue areas and has minimal values at exceptional points (EPs). By tuning the relative angle β, periodic photon blockade (PB) can be implemented. Additionally, we find that the robustness of the Kerr-nonlinear strength of the CW mode is enhanced. Similarly, the antibunching effect of the CCW mode and magnon mode appear in the curved dark blue areas, and the EPs emerge periodically. These results offer a potential approach to achieve an antibunching-to-bunching light switch by harnessing the chiral exceptional points.

VI. IMPLEMENTATION IN YIG MICRORESONATOR

Recent groundbreaking experiments have demonstrated that a hybrid optomagnonics system, which simultaneously supports magnon resonances and whispering gallery modes (WGMs) can be realized [67]. While the Kittel mode (the homogeneous magnetic mode) is the simplest one to probe and externally tune, its status as a bulk mode results in suboptimal overlap with optical WGMs that reside near the surface. Furthermore, nanotips can be fabricated through wet etching of tapered fibers, and their relative position and effective size can be controlled by the nanotips themselves [81].

In our current proposal, the photon-magnon blockade effect is achieved under the condition $g_j \ll \kappa_j$, which reduces the experimental requirements typically associated with optomagnonics systems. The unique properties of the cavity enable more effective utilization of the YIG crystal's high spin density for cavity optomagnonics experiments. Supported by current experimental technology, YIG spheres can be highly polished with diameters as small as 250 μm, and the quality factor of the WGMs optical mode can reach

3×10^6 [5]. Therefore, for YIG with characteristic frequencies $\omega_m \approx 1$–10 GHz, the condition on the coupling is easily fulfilled $\omega_m/GS \ll 1$, whereas κ_j can be estimated to be $\approx 10^{10}$ Hz and the coupling G gives the magnon precession frequency shift per photon [67]. It decreases for larger magnon mode volume, in contrast to GS, which describes the overall optical shift for saturated spin S [67]. Moreover, the perturbations induced by the nanotips are chosen as $\epsilon_1/\kappa = 1.5 - i0.1, \epsilon_2/\kappa = 1.485 - i0.14$, which have been experimentally achieved [48,76]. Consequently, our scheme can be implemented under practical experimental conditions. We have demonstrated chiral modes in YIG microcavities via geometry-induced non-Hermitian mode couplings. The underlying physical mechanism that enables chirality and directional emission is the strong asymmetric backscattering in the vicinity of an EP that universally occurs in all open physical systems.

VII. CONCLUSION

In summary, we propose a periodic photon-magnon blockade in a hybrid optomagnonics system where a YIG microresonator coupled to two silica nanotips. By adjusting the relative angle of two nanotips, quantum correlations between magnons and photons can be finely tuned, transitioning between antibunching and bunching regimes or vice versa. The exceptional points also reveal a completely asymmetric coupling between the CW and CCW modes. Additionally, we demonstrate the feasibility of achieving simultaneous photon-magnon blockade in the weak optomagnonic coupling regime. As a result, the robustness of the Kerr-nonlinear strength for the CW, CCW, and magnon modes, where the strong kerr nonlinearity of magnon mode is not required. By steering the system towards or away from an exceptional point, we enable chiral control and allow asymmetric coupling. This feature suggests a potential method for developing tunable single photon-magnon sources and antibunching-to-bunching light switches.

[1] J. W. Rao, B. Yao, C. Y. Wang, C. Zhang, T. Yu, and W. Lu, Phys. Rev. Lett. **130**, 046705 (2023).

[2] O. O. Soykal and M. E. Flatté, Phys. Rev. Lett. **104**, 077202 (2010).

[3] J. Li, S.-Y. Zhu, and G. S. Agarwal, Phys. Rev. Lett. **121**, 203601 (2018).

[4] L. Bai, M. Harder, Y. P. Chen, X. Fan, J. Q. Xiao, and C.-M. Hu, Phys. Rev. Lett. **114**, 227201 (2015).

[5] X. Zhang, C.-L. Zou, L. Jiang, and H. X. Tang, Sci. Adv. **2**, e1501286 (2016).

[6] T. Wang, C.-H. Bai, D.-Y. Wang, S. Liu, S. Zhang, and H.-F. Wang, Phys. Rev. A **104**, 013721 (2021).

[7] Y.-H. Kang, Y.-H. Chen, X. Wang, J. Song, Y. Xia, A. Miranowicz, S.-B. Zheng, and F. Nori, Phys. Rev. Res. **4**, 013233 (2022).

[8] Y.-L. Fang, J.-L. Zhao, D.-X. Chen, Y.-H. Zhou, Y. Zhang, Q.-C. Wu, C.-P. Yang, and F. Nori, Phys. Rev. Res. **4**, 033022 (2022).

[9] Y.-H. Chen, A. Miranowicz, X. Chen, Y. Xia, and F. Nori, Phys. Rev. Appl. **18**, 064059 (2022).

[10] P. Hyde, B. M. Yao, Y. S. Gui, G.-Q. Zhang, J. Q. You, and C.-M. Hu, Phys. Rev. B **98**, 174423 (2018).

[11] A. A. J. Holanda, D. S. Maior, and S. M. Rezende, Nat. Phys. **14**, 500 (2018).

[12] Z.-X. Liu, C. You, B. Wang, H. Xiong, and Y. Wu, Opt. Lett. **44**, 507 (2019).

[13] Z. Toklikishvili, L. Chotorlishvili, R. Khomeriki, V. Jandieri, and J. Berakdar, Phys. Rev. B **107**, 115126 (2023).

[14] X.-L. Hei, P.-B. Li, X.-F. Pan, and F. Nori, Phys. Rev. Lett. **130**, 073602 (2023).

[15] Y.-P. Wang, G.-Q. Zhang, D. Zhang, X.-Q. Luo, W. Xiong, S.-P. Wang, T.-F. Li, C.-M. Hu, and J. Q. You, Phys. Rev. B **94**, 224410 (2016).

[16] Y. Tabuchi, S. Ishino, T. Ishikawa, R. Yamazaki, K. Usami, and Y. Nakamura, Phys. Rev. Lett. **113**, 083603 (2014).

[17] X. Zhang, N. Zhu, C.-L. Zou, and H. X. Tang, Phys. Rev. Lett. **117**, 123605 (2016).

[18] X. Zhang, C.-L. Zou, L. Jiang, and H. X. Tang, Phys. Rev. Lett. **113**, 156401 (2014).

[19] J. W. Rao *et al.*, Nat. Commun. **10**, 2934 (2019).

[20] J. W. Rao, Y. P. Wang, Y. Yang, T. Yu, Y. S. Gui, X. L. Fan, D. S. Xue, and C.-M. Hu, Phys. Rev. B **101**, 064404 (2020).

[21] M. Goryachev, W. G. Farr, D. L. Creedon, Y. Fan, M. Kostylev, and M. E. Tobar, Phys. Rev. Appl. **2**, 054002 (2014).

[22] H. Huebl, C. W. Zollitsch, J. Lotze, F. Hocke, M. Greifenstein, A. Marx, R. Gross, and S. T. B. Goennenwein, Phys. Rev. Lett. **111**, 127003 (2013).

[23] W. Xiong, M. Wang, G.-Q. Zhang, and J. Chen, Phys. Rev. A **107**, 033516 (2023).

[24] T.-R. Bai, Z.-D. Chen, J.-Q. Zhang, D. Yan, Z.-W. He, S. Zhang, J. Zhao, and Y. Yu, Phys. Rev. A **107**, 033522 (2023).

[25] J.-k. Xie, S.-l. Ma, and F.-l. Li, Phys. Rev. A **101**, 042331 (2020).

[26] Z.-X. Liu, H. Xiong, and Y. Wu, Phys. Rev. B **100**, 134421 (2019).

[27] C. Zhao, X. Li, S. Chao, R. Peng, C. Li, and L. Zhou, Phys. Rev. A **101**, 063838 (2020).

[28] K. Wu, W.-X. Zhong, G.-L. Cheng, and A.-X. Chen, Phys. Rev. A **103**, 052411 (2021).

[29] X. Li, X. Wang, Z. Wu, W.-X. Yang, and A. Chen, Phys. Rev. B **104**, 224434 (2021).

[30] Z. Haider, S. Qamar, and M. Irfan, Phys. Rev. A **107**, 043702 (2023).

[31] C. W. J. Beenakker, Phys. Rev. B **44**, 1646 (1991).

[32] Y. Wang, J.-L. Wu, J.-X. Han, Y. Xia, Y.-Y. Jiang, and J. Song, Phys. Rev. Appl. **17**, 024009 (2022).

[33] P. Rabl, Phys. Rev. Lett. **107**, 063601 (2011).

[34] J.-Q. Liao and F. Nori, Phys. Rev. A **88**, 023853 (2013).

[35] B. Sarma and A. K. Sarma, Phys. Rev. A **96**, 053827 (2017).

[36] Q. Bin, X.-Y. Lü, S.-W. Bin, and Y. Wu, Phys. Rev. A **98**, 043858 (2018).

[37] D.-Y. Wang, C.-H. Bai, X. Han, S. Liu, S. Zhang, and H.-F. Wang, Opt. Lett. **45**, 2604 (2020).

[38] Y.-H. Kang, Z.-C. Shi, J. Song, and Y. Xia, Phys. Rev. A **102**, 022617 (2020).

[39] N. Didier, S. Pugnetti, Y. M. Blanter, and R. Fazio, Phys. Rev. B **84**, 054503 (2011).

[40] D.-Y. Wang, C.-H. Bai, S. Liu, S. Zhang, and H.-F. Wang, New J. Phys. **22**, 093006 (2020).

[41] H. Jing, S. K. Özdemir, X.-Y. Lü, J. Zhang, L. Yang, and F. Nori, Phys. Rev. Lett. **113**, 053604 (2014).

[42] C. Yin and Z. Cao, Phys. Rev. A **80**, 064102 (2009).

[43] C. Zhai, R. Huang, H. Jing, and L.-M. Kuang, Opt. Express **27**, 27649 (2019).

[44] Y. Guo, K. Li, W. Nie, and Y. Li, Phys. Rev. A **90**, 053841 (2014).

[45] D.-Y. Wang, C.-H. Bai, Y. Xing, S. Liu, S. Zhang, and H.-F. Wang, Phys. Rev. A **102**, 043705 (2020).

[46] S. Liu, Y.-H. Chen, Y. Wang, Y.-H. Kang, Z.-C. Shi, J. Song, and Y. Xia, Phys. Rev. A **106**, 042430 (2022).

[47] D.-Y. Wang, C.-H. Bai, S. Liu, S. Zhang, and H.-F. Wang, Phys. Rev. A **99**, 043818 (2019).

[48] W. Chen, S. K. Özdemir, G. Zhao, J. Wiersig, and L. Yang, Nature (London) **548**, 192 (2017).

[49] Y. Xu, J.-Y. Liu, W. Liu, and Y.-F. Xiao, Phys. Rev. A **103**, 053501 (2021).

[50] C. Shen, X. Zhu, J. Li, and S. A. Cummer, Phys. Rev. B **100**, 054302 (2019).

[51] X. Zhao, Y. Xing, L. Qi, S. Liu, S. Zhang, and H.-F. Wang, New J. Phys. **23**, 073043 (2021).

[52] J.-X. Han, J.-L. Wu, Y. Wang, Y. Xia, Y.-Y. Jiang, and J. Song, Phys. Rev. B **105**, 064431 (2022).

[53] L. Ferrier, P. Bouteyre, A. Pick, S. Cueff, N. H. M. Dang, C. Diederichs, A. Belarouci, T. Benyattou, J. X. Zhao, R. Su, J. Xing, Q. Xiong, and H. S. Nguyen, Phys. Rev. Lett. **129**, 083602 (2022).

[54] M. Kang, J. Chen, and Y. D. Chong, Phys. Rev. A **94**, 033834 (2016).

[55] A. Banerjee and A. Narayan, Phys. Rev. B **102**, 205423 (2020).

[56] T.-X. Lu, H. Zhang, Q. Zhang, and H. Jing, Phys. Rev. A **103**, 063708 (2021).

[57] J. Wiersig, Phys. Rev. A **84**, 063828 (2011).

[58] C. Dembowski, H.-D. Gräf, H. L. Harney, A. Heine, W. D. Heiss, H. Rehfeld, and A. Richter, Phys. Rev. Lett. **86**, 787 (2001).

[59] T. Gao, E. Estrecho, K. Y. Bliokh, T. C. H. Liew, M. D. Fraser, S. Brodbeck, M. Kamp, C. Schneider, S. Höfling, Y. Yamamoto, F. Nori, Y. S. Kivshar, A. G. Truscott, R. G. Dall, and E. A. Ostrovskaya, Nature (London) **526**, 554 (2015).

[60] C. Dembowski, B. Dietz, H.-D. Gräf, H. L. Harney, A. Heine, W. D. Heiss, and A. Richter, Phys. Rev. Lett. **90**, 034101 (2003).

[61] H. Cartarius, J. Main, and G. Wunner, Phys. Rev. Lett. **99**, 173003 (2007).

[62] S.-B. Lee, J. Yang, S. Moon, S.-Y. Lee, J.-B. Shim, S. W. Kim, J.-H. Lee, and K. An, Phys. Rev. Lett. **103**, 134101 (2009).

[63] M. Brandstetter, M. Liertzer, C. Deutsch, P. Klang, J. Schöberl, H. E. Türeci, G. Strasser, K. Unterrainer, and S. Rotter, Nat. Commun. **5**, 4034 (2014).

[64] R. Huang, S. K. Özdemir, J.-Q. Liao, F. Minganti, L.-M. Kuang, F. Nori, and H. Jing, Laser Photonics Rev. **16**, 2100430 (2022).

[65] W. Zhang, D.-Y. Wang, C.-H. Bai, T. Wang, S. Zhang, and H.-F. Wang, Opt. Express **29**, 11773 (2021).

[66] T. Holstein and H. Primakoff, Phys. Rev. **58**, 1098 (1940).

[67] S. Viola Kusminskiy, H. X. Tang, and F. Marquardt, Phys. Rev. A **94**, 033821 (2016).

[68] S. Sharma, Y. M. Blanter, and G. E. W. Bauer, Phys. Rev. B **96**, 094412 (2017).

[69] J. Graf, H. Pfeifer, F. Marquardt, and S. Viola Kusminskiy, Phys. Rev. B **98**, 241406(R) (2018).

[70] S. Sharma, B. Z. Rameshti, Y. M. Blanter, and G. E. W. Bauer, Phys. Rev. B **99**, 214423 (2019).

[71] Z. Haghshenasfard and M. G. Cottam, Phys. Rev. B **101**, 144438 (2020).

[72] J. Zou, S. K. Kim, and Y. Tserkovnyak, Phys. Rev. B **101**, 014416 (2020).

[73] R.-C. Shen, J. Li, Z.-Y. Fan, Y.-P. Wang, and J. Q. You, Phys. Rev. Lett. **129**, 123601 (2022).

[74] G.-Q. Zhang, Z. Chen, W. Xiong, C.-H. Lam, and J. Q. You, Phys. Rev. B **104**, 064423 (2021).

[75] H. Lü, C. Wang, L. Yang, and H. Jing, Phys. Rev. Appl. **10**, 014006 (2018).

[76] B. Peng, Ş. K. Özdemir, M. Liertzer, W. Chen, J. Kramer, H. Yılmaz, J. Wiersig, S. Rotter, and L. Yang, Proc. Natl. Acad. Sci. USA **113**, 6845 (2016).

[77] A. Sergi and K. G. Zloshchastiev, Int. J. Mod. Phys. B **27**, 1350163 (2013).

[78] D. C. Brody and E.-M. Graefe, Phys. Rev. Lett. **109**, 230405 (2012).

[79] F. Minganti, A. Miranowicz, R. W. Chhajlany, and F. Nori, Phys. Rev. A **100**, 062131 (2019).

[80] W. Chen, M. Abbasi, Y. N. Joglekar, and K. W. Murch, Phys. Rev. Lett. **127**, 140504 (2021).

[81] W.-L. Xu, Y.-P. Gao, C. Cao, T.-J. Wang, and C. Wang, Phys. Rev. A **102**, 043519 (2020).